**RESEARCH ARTICLE**

# Ballistic behavior of plain and reinforced concrete slabs under high velocity impact

Chahmi OUCIF[a*], Luthfi Muhammad MAULUDIN[a,b], Farid Abed[c]

[a] *Institute of Structural Mechanics, Bauhaus-Universität Weimar, Weimar D-99423, Germany*

[b] *Teknik Sipil, Politeknik Negeri Bandung, Gegerkalong Hilir Ds.Ciwaruga, Bandung 40012, Indonesia*

[c] *Department of Civil Engineering, American University of Sharjah, Sharjah 26666, United Arab Emirates*

[*] *Corresponding author. E-mail: chahmi.oucif@uni-weimar.de*

**ABSTRACT**    This work presents a numerical simulation of ballistic penetration and high velocity impact behavior of plain and reinforced concrete slabs. In this paper, we focus on the comparison of the performance of the plain and reinforced concrete slabs of unconfined compressive strength 41 MPa under ballistic impact. The concrete slab has dimensions of 675 mm × 675 mm × 200 mm, and is meshed with 8-node hexahedron solid elements in the impact and outer zones. The ogive-nosed projectile is considered as rigid element that has a mass of 0.386 kg and a length of 152 mm. The applied velocities vary between 540 and 731 m/s. 6 mm of steel reinforcement bars were used in the reinforced concrete slabs. The constitutive material modeling of the concrete and steel reinforcement bars was performed using the Johnson-Holmquist-2 damage and the Johnson-Cook plasticity material models, respectively. The analysis was conducted using the commercial finite element package Abaqus/Explicit. Damage diameters and residual velocities obtained by the numerical model were compared with the experimental results and effect of steel reinforcement and projectile diameter were studies. The validation showed good agreement between the numerical and experimental results. The added steel reinforcements to the concrete samples were found efficient in terms of ballistic resistance comparing to the plain concrete sample.

**KEYWORDS**    Johnson-Holmquist-2, Johnson-Cook, reinforced concrete, damage, impact loads

## 1   Introduction

Concrete is the most advantageous material used in the construction of structures due to its resistance of the effect of blast [1,2]. It becomes ductile when is appropriately reinforced, especially under tensile loads [3–7], and is transformed into the most suitable material in the construction of nuclear and protective infrastructures due to the improvement in its strength and performance. The study of impact behavior of reinforced concrete structures has received much attention over the last decades [8–13].

Many experimental studies have been conducted on the description of the impact behavior of reinforced concrete (RC) structures, in which the results showed that the RC structures exhibit high resistance when high concrete strength is used [14,15]. In Ref. [16], it was exceptionally revealed that the increase in the compressive strength influences minorly the impact resistance of the RC concrete slab. Borvik et al. [17] studied experimentally the ballistic penetration of steel fiber reinforced high-performance concrete slabs penetrated by steel projectiles. A low increase of 20% in the ballistic limit velocity was obtained when the unconfined compressive strength of the concrete increases. Cai et al. [18] studied the behavior of RC concrete samples under dynamic tension. Li et al. [19] studied the blast resistance of concrete slabs reinforced with steel fibers and steel bars. The results showed promising resistance of concrete slabs reinforced with hybrid steel fibers and steel bars. Liu et al. [20] performed experimental and numerical investigations on impact resistance of reactive powder concrete slabs reinforced with different steel bars configurations. The influence of mechanical properties of steel bars on the impact resistance of the samples was considered. An enhancement in the

impact resistance in terms in decrease of depth of penetration due steel bars reinforcement was found. Isaac et al. [21] carried out experimental tests on reinforced concrete beams in order to measure the rate of the force that propagate from the impact zone. The results revealed that there is a link between the ratio span/depth and the velocity that makes the force propagates from the impact point. Othman and Marzouk [22] studied the effect of steel reinforcement distribution on the dynamic behavior of the reinforced concrete plates subjected to impact loads. It was found that in the case of low velocity impact the impact energy in unaffected by the ratio and distribution of the steel reinforcement, while the crack pattern and failure mode are affected by only the distribution of the steel reinforcement.

Besides the experimental investigations, the implementation of numerical models is indispensable to understand the impact behavior of RC structures. Thai et al. [23] proposed new empirical formulas to predict the penetration depth and perforation thickness of reinforced concrete panels subjected to impact loads with taking into account the effect of reinforcement. It was found that the proposed formulas are valid only in the range of 50 to 250 m/s of the impact velocity. Feng et al. [24] used the Lattice Discrete Particles Model (LDPM) to simulate the impact behavior of RC panels subjected to hard projectile penetration. In conjunction with LDPM the sliding friction model for the interaction steel-bars/concrete was used. Thai and Kim [25] studied numerically the damage of RC columns subjected to blast loading. The results revealed that the stocky columns show local damage, while the slender columns show local and global damages. Zhao et al. [26] simulated the influence of span of RC beams on the impact behavior. The results revealed that localization features appear at an early stage of the impact behavior. In Ref. [27], the authors used a modified version of the Johnson-Holmquist (HJC) damage model to describe the cratering and scabbing in concrete slabs subjected to impact loads. For the same purpose, a modified version of Karagozian and Case concrete model was used in Ref. [28]. The same authors proposed a new material for concrete subjected to intense dynamic loads with the application of three-invariant failure surface and based on the level of current damage [29]. In Ref. [30], a new mesh-free method was implemented for the description of the behavior of brittle materials subjected to an explosion. Several other simulations were carried out to demonstrate the applicability of the mesh-free method and advances in modeling of fracture and damage [31–60]. Other investigations were based on multi-scale modeling [61–66] and phase field modeling [67–76].

Few numerical investigations were performed to study the behavior of concrete slabs under impact loads and reinforced with different configurations of longitudinal steel reinforcements mixed with transverse steel reinforcements. In the present paper, numerical simulation of plain

and reinforced concrete slabs penetrated by rigid ogive-nosed steel projectile is performed. The Johnson-Holmquist-2 damage model (JH-2) is considered for concrete material, while steel reinforcements are modeled using the Johnon-Cook plasticity model. The projectile is modeled as analytical rigid element with a mass assigned in a reference point. The contact between the projectile and reinforcec concrete slab is defined based on general contact surface with nodal erosion. Validation is performed by comparing the equivalent cratering damage diameter and residual velocity obtained by the numerical model are compared with the experimental results. In addition, the effect of steel reinforcements and projectile diameter on the ballistic resistance of concrete slabs is also studied.

## 2  Material models

The concrete material is simulated in this paper using the JH-2. The JH-2 is the second version of the Johnson-Holmquist (JH-1) ceramic model [77], that is able to simulate the impact behavior of brittle materials such as dilatation, pressure-strength dependence, strain-rate effect resulted by damage [77]. According to the JH-2 model, the yield strength degrades with damage accumulation whereas in the JH-1 model the yield strength degrades when critical damage is reached. The strength is defined in terms of the equivalent stress as follows:

$$\sigma^* = \sigma_i^* - D(\sigma_i^* - \sigma_f^*), \tag{1}$$

where $\sigma_i^*$ is the normalized intact equivalent stress, $D$ is the damage variable, and $\sigma_f^*$ is the normalized fractured equivalent stress. It is important to point out that the intact and fully damaged materials are represented by the damage values $D = 0$ and $D = 1$, respectively. The normalization of the term in Eq. (1) to the equivalent stress at the Hugoniot Elastic Limit (HEL) can also be used to define the equations of the strength, which will correspond to the one-dimensional shock wave that exceeds the elastic limit as defines in Eq. (2), and the normalized equation as presents Eq. (3):

$$\sigma_{HEL} = \frac{3}{2}(HEL - P_{HEL}), \tag{2}$$

$$\sigma^* = \frac{\sigma}{\sigma_{HEL}}, \tag{3}$$

where $P_{HEL}$ is the pressure at the HEL. According to the JH-2 model, the equation of the strength in the case of the undamaged and fully damaged material states is assumed to be, respectively, written as function of pressure and strain rate as follows:

$$\sigma_i^* = A(P^* + T^*)^N(1 + C\ln\dot{\varepsilon}^*)\sigma_i^{max}, \tag{4}$$

$$\sigma_f^* = B(P^*)^M(1 + C\ln\dot{\varepsilon}^*)\sigma_f^{max}, \tag{5}$$

where $A$, $B$, $C$, $M$, and $N$ are the material parameters, $\sigma_i^{\max}$ and $\sigma_f^{\max}$ are the strengths limits.

The normalized pressure is defined as

$$P^* = \frac{P}{P_{HEL}}, \tag{6}$$

where $P$ is the actual pressure. The normalized maximum tensile hydrostatic pressure is also written as

$$T^* = \frac{T}{T_{HEL}}, \tag{7}$$

where $T$ is the maximum tensile pressure supported by the material and $T_{HEL}$ is the tensile pressure at the HEL. The strain rate is is defined as $\dot{\varepsilon}^{pl} = \dot{\varepsilon}^{pl}/\dot{\varepsilon}_0$, and $\dot{\varepsilon}^{pl}$ is the equivalent plastic strain rate. Damage accumulation is used in JH-2 model similarly to the Johnson-Cook model in addition to the assumption that damage increases along with the plastic strain as follows:

$$D = \sum \frac{\Delta \bar{\varepsilon}^{pl}}{\bar{\varepsilon}_f^{pl}(P)}, \tag{8}$$

$$\bar{\varepsilon}^{pl} = D_1(P^* + T^*)^{D_2}, \quad \bar{\varepsilon}_{f,\min}^{pl} \leqslant \bar{\varepsilon}^{pl} \leqslant \bar{\varepsilon}_{f,\max}^{pl}. \tag{9}$$

It is important to point out that $\Delta \bar{\varepsilon}^{pl}$ is the increment of the equivalent plastic strain, and $\bar{\varepsilon}_f^{pl}(P)$ is the equivalent plastic strain at failure. $D_1$ and $D_2$ are material constants. To limit the minimum and maximum values of the fracture strain, the parameters $\bar{\varepsilon}_{f,\min}^{pl}$ and $\bar{\varepsilon}_{f,\max}^{pl}$ are introduced. The pressure-volume relationship of the brittle materials is defined as
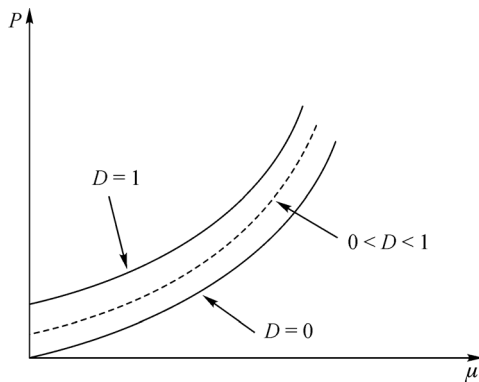


**Fig. 1** Pressure-volumetric strain relationship of the JH-2 model.

$$P = \begin{cases} K_1\mu + K_2\mu^2 + K_3\mu^3, & \text{if } \mu \geqslant 0 \text{ (compression)}, \\ K_1\mu, & \text{if } \mu < 0 \text{ (tension)}. \end{cases} \tag{10}$$

where $K_1$, $K_2$, $K_3$ are material constants, and $\mu = \rho/\rho_0 - 1$

with $\rho$ and $\rho_0$ representing the current and reference densities, respectively. An additional pressure increment $\Delta P$ in the case of material failure, which is expressed as

$$P = K_1\mu + K_2\mu^2 + K_3\mu^3 + \Delta P. \tag{11}$$

The determination of the pressure increment is determined based on the energy consideration. Due to the decrease in strength the deviatoric elastic energy $\Delta U$ decreases in the case of damaged material. Figure 1 shows the relationship pressure-volumetric strain according to the JH-2 model.

The decrease of the elastic energy is converted into the potential energy by the increase of the pressure increment $\Delta P$, such that

$$\Delta P_{t+\Delta t} = -K_1\mu_{t+\Delta t}$$
$$+ \sqrt{(K_1\mu_{t+\Delta t} + \Delta P_t)^2 + 2\beta K_1 \Delta U}, \tag{12}$$

where $\beta$ is the fraction of the elastic energy increase converted to potential energy ($0 \leqslant \beta \leqslant 1$).

In the present work, the parameters of the JH-2 model based on HEL are calculated, while the parameters based on equation of state, strength and damage are taken from the literature. The HEL for brittle materials is calculated using Eq. (13) [78]:

$$HEL = \frac{1-\nu}{(1-\nu)^2}f_c, \tag{13}$$

where $\nu$ is the Poisson's ratio and $f_c$ is the compressive strength. Afterward, the pressure at $HEL$ is calculated using the following expression:

$$P_{HEL} = HEL\left(1 - \frac{4G}{3k + 4G}\right), \tag{14}$$

where $G$ and $k$ are the shear and bulk moduli, respectively. The parameters related to the strength, damage, and equation of state are taken from Refs. [27,77]. Table 1 illustrates the material parameters of the JH-2 model for unconfined compressive strength concrete 41 MPa.

The steel reinforcement are simulated in the present work using the Johnson-Cook plasticity model that is capable to simulate the strain hardening, softening, plastic flow, yielding of metals [79]. According to the Johnson-Cook model the Von Mises stress is expressed as a function of the equivalent strain $\bar{\varepsilon}^{pl}$, equivalent plastic strain rate $\dot{\varepsilon}^{pl}$, and temperature $T$ as follows:

$$\bar{\sigma} = \left(A + B(\bar{\varepsilon}^{pl})^n\right)\left[1 + C\ln\left(\dot{\varepsilon}^{pl}/\dot{\varepsilon}_0^{pl}\right)\right](1 - T^{*m}), \tag{15}$$

where $A$, $B$, $C$, and $M$ are constants; $\dot{\varepsilon}^{pl}/\dot{\varepsilon}_0^{pl}$ and $T^*$ are the normalized equivalent plastic strain rate and the temperature, respectively. The temperature $T^*$ is expressed as follows:

**Table 1**  Material parameters of the concrete material

| parameters | value |
|---|---|
| $P$ (kg/m³) | 2440 |
| $G$ (GPa) | 14.86 |
| $v$ | 0.15 |
| $A$ | 0.3 |
| $B$ | 2 |
| $n$ | 0.75 |
| $C$ | 0.007 |
| $m$ | 0.61 |
| $\dot{\varepsilon}_0$ | 1 |
| $S_{max}$ | 7 |
| $T$ (GPa) | 0.004 |
| $\bar{\varepsilon}_{f,min}^{pl}$ | 0.001 |
| $\bar{\varepsilon}_{f,max}^{pl}$ | 1 |
| $P_{HEL}$(MPa) | 33.43 |
| $D_1$ | 0.04 |
| $D_2$ | 1 |
| $K_1$ (GPa) | 17.12 |
| $K_2$ (GPa) | −171 |
| $K_3$ (GPa) | 208 |
| $HEL$ (MPa) | 71.12 |
| $f_c$ | 41 |

**Table 2**  Material parameters of the steel reinforcement [80]

| parameters | value |
|---|---|
| $\rho$ (kg/m³) | $2\times10^{11}$ |
| $v$ | 0.33 |
| $A$ | 490 |
| $B$ | 807 |
| $n$ | 0.73 |
| $m$ | 0.94 |
| melting temperature (Kelvin) | 1800 |
| transition temperature (Kelvin) | 293 |
| $d_1$ | 0.0705 |
| $d_2$ | 1.732 |
| $d_3$ | −0.54 |
| $d_4$ | −0.015 |
| $d_5$ | 0 |
| strain rate ($S^{-1}$) | 0.0005 |

$$T^* = (T - T_r)/(T_{melt} - T_r), \qquad (16)$$

where $T$ is the current temperature, $T_{melt}$ is the melting temperature, and $T_r$ is the room temperature. The expression of the fracture according to the Johnson-Cook model is defined in terms of the equivalent failure strain as follows:

$$\bar{\varepsilon}_D^{pl} = [d_1 + d_2 \mathrm{ex}(-d_3\eta)]\left[1 + d_4\ln\left(\dot{\varepsilon}_0^{pl}/\varepsilon_0^{pl}\right)\right](1 + d_5T^*), \qquad (17)$$

where $\eta = -p/\bar{\sigma}$ is the stress triaxiality, $p$ is the pressure and $d_1$, $d_2$, $d_3$, $d_4$, $d_5$ are constants. According to the Johnson-Cook model, the damage is assumed to occur when the damage variable $D$ reaches its limit value of 1.0. The Johnson-Cook material parameters for steel reinforcement used in the present work are presented in Table 2 [80].

## 3   Numerical simulation of RC targets

The Johnson-Holmquist-2 and Johnson-Cook material models are applied on the penetration experiment of reinforced concrete by Wu et al. [81] and incorpo-rated into the commercial finite element package Abaqus/

Explicit. The numerical models consists of the study of the impact behavior of reinforced concrete slabs of dimensions 675 mm × 675 mm × 200 mm simulated as three dimensional deformable solid penetrated with an ogive-nosed steel projectile of 152 mm of length, 25.3 mm of diameter, and 3.00 of the caliber-radius-head (CRH) ratio (Fig. 2). The projectile is simulated as rigid element with 0.386 kg of mass assigned at a reference point with striking velocities ranging from 540 to 731 m/s. The steel reinforcements are simulated as truss elements of diameter 6 mm and embedded into the concrete solid body. The embedded truss elements to the concrete makes the nodes of the steel bars kinematically constrained to the nodes of the concrete solid body. The distribution of the steel reinforcement bars is illustrated in Fig. 3. General contact surface with nodal erosion between the projectile and the RC concrete slab is considered. Using nodal erosion, the nodes of the element based surfaces are removed from the contact domain once the contact faces are eroded. All the edges of the concrete slab are fixed in all directions in terms of translation and rotation. In addition, the reference point of the hard projectile is fixed in all directions in terms of translation and rotation expect the translation in the impact direction. A circular partition of 20 mm was created at the impact location in order to refine the mesh. Three dimensional eight node reduced integration (C3D8R) element was adopted for all the regions with 1 mm × 1 mm × 1 mm of mesh at the impact location and 3.5 mm × 3.5 mm × 3.5 mm of mesh at the rest of the sample. A mesh convergence study of element sizes of 0.8, 0.9, 1, 1.5, and 2 mm for the RC slab at the impact location subjected to the projectile penetration at the striking velocity of 641 m/s is performed. The residual velocity of the projectile with different mesh sizes is compared as shows in Fig. 4. It is found that the residual velocity increases with the
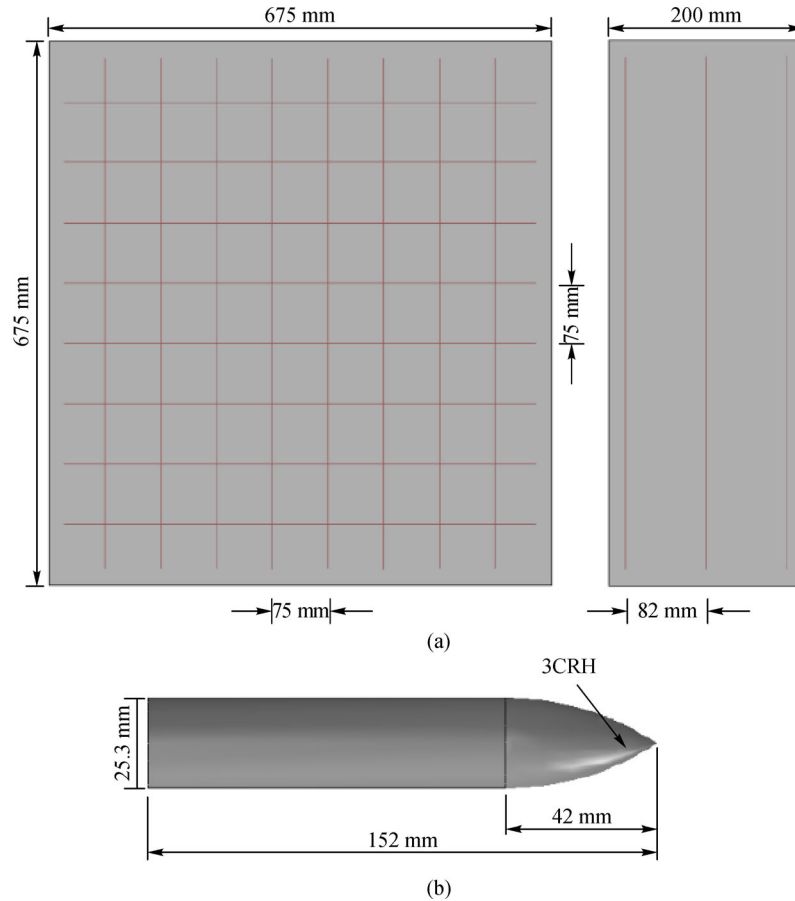
**Fig. 2**  (a) Reinforced concrete slab and (b) projectile geometries.
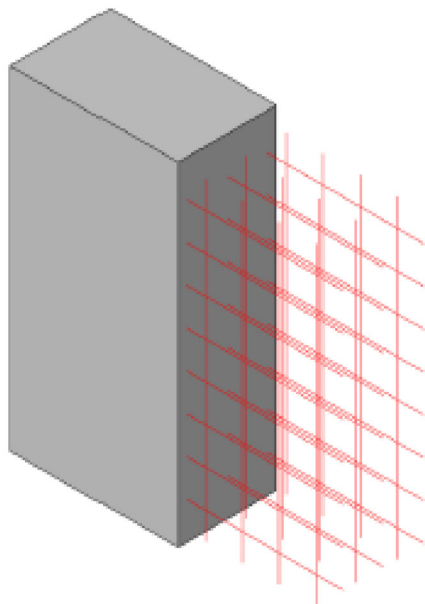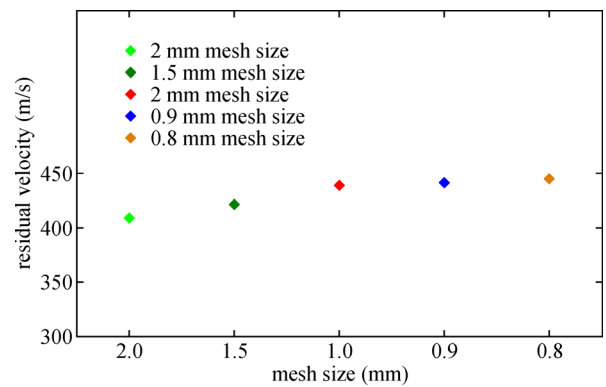


**Fig. 3**  FE model of steel reinforcement configuration.



**Fig. 4**  Mesh convergence study with various mesh sizes.

441.31 to 439.36 m/s indicating a slight difference of 0.44%. Thus, it is believed that using the mesh size of 1 mm provides reasonable results in the numerical simulation with less computational time. Two node three dimensional truss elements (T3D2) with mesh size of 2 mm were considered for the vertical, horizontal and transverse steel reinforcements, and four node three dimensional bilinear rigid quadrilateral (R3D4) meshes with size of 2 mm were considered for the projectile.

decrease of the element size. When the mesh size increases from 0.9 to 1 mm, the residual velocity decreases from
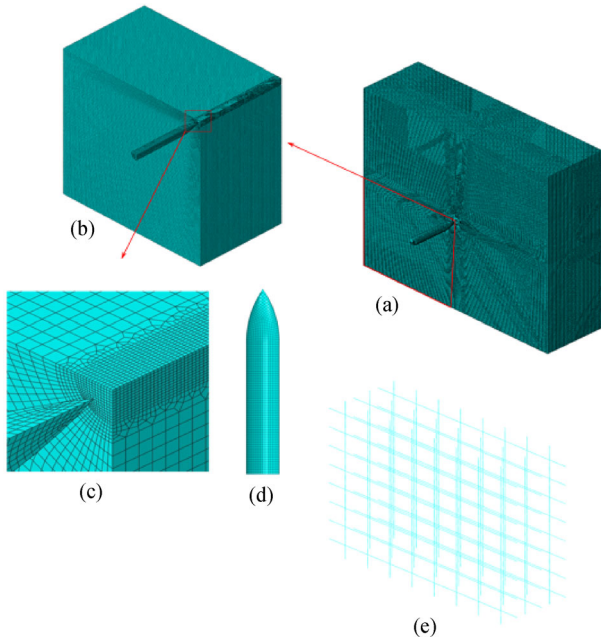
**Fig. 5** E meshing of (a) total geometry, (b) quarter of geometry, (c) impact location details, (d) projectile, and (e) steel reinforcement.

Figure 5 illustrates the finite element meshing of the reinforced concrete slab. The mesh of the concrete slab was generated in the aim to obtain accurate results with less time consuming of the finite element analysis.

## 4  Model validation

The JH-2 model for concrete and Johnson-Cook model for steel reinforcement are incorporated into Abaqus/Explicit. The penetration experiment of reinforced concrete slabs by Wu et al. [81] was simulated. In this section, the comparison of the cratering and scabbing damages of the reinforced concrete slabs and the residual velocity of the projectile is performed. The dimensions of the diameters of front and back craters formed in the RC slabs due to the penetration of the hard projectile are calculated. The equivalent damage diameter $D_m$ of the front and back of craters is calculated as $(D_m = D_1 + D_2 + D_3 + D_4)/4$ in which $D_1$, $D_2$, $D_3$, and $D_4$ are shown in Fig. 6. Figure 7 shows the comparison of the numerical and experimental cratering and scabbing damages of the reinforced concrete slab subjected to the impact velocity 640 m/s. The equivalent diameters of the front face in the experimental and numerical studies are found to be 275 and 277 mm, respectively, while they are, respectively, 242.5 and 286 mm in the back face. Differences of 0.72% and 15% in the front and back faces are respectively obtained. In the whole, it can be observed that the damages at the front and back faces predicted numerically are in good agreement
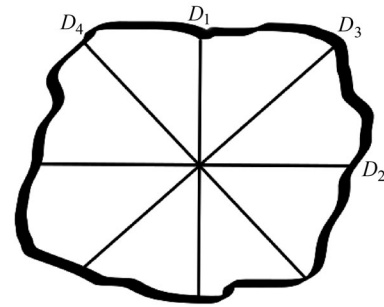


**Fig. 6** Calculation of equivalent diameter of front and back craters.
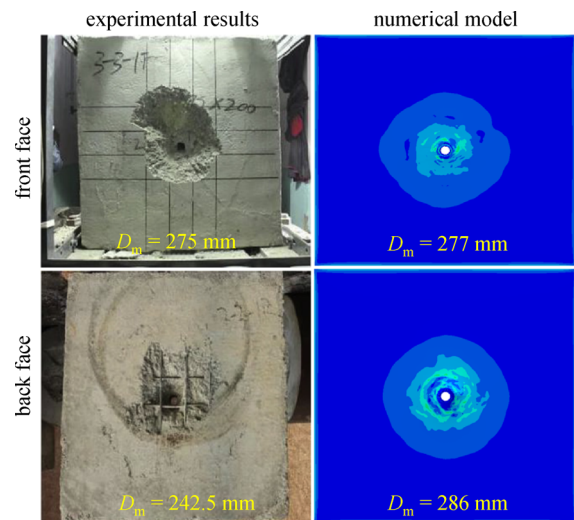


**Fig. 7** Experimental and numerical comparison of front and back damages at impact velocity of 641 m/s.
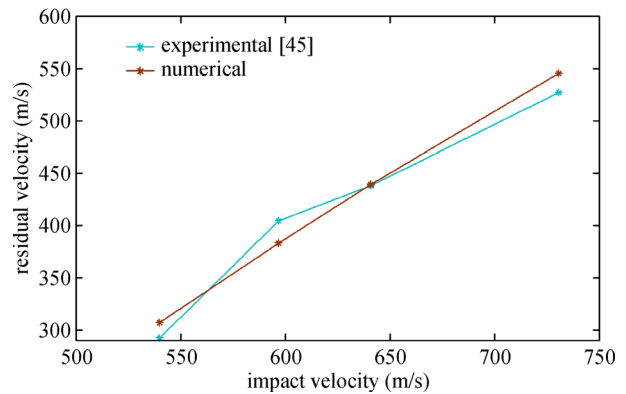


**Fig. 8** Comparison of numerical and experimental residual velocities.

with the experimental results. Figure 8 shows the predicted residual velocity compared with the experimental residual velocity corresponding to the impact velocities 540, 597,

641, and 731 m/s. It can be seen that the numerical model reproduces well the residual velocity comparing to the experimental results.

# 5   Effect of steel reinforcement

In this section, the effect of steel reinforcement on the impact resistance and cratering damage is analyzed. The cratering damage and residual velocity of plain, reinforced, and additionally reinforced concrete slabs are compared under the striking velocities 540, 597, 641 and 731 m/s. The equivalent damage diameter ($d_m$) is calculated in the front and back surfaces as the average diameter values ($d_1$, $d_2$, $d_3$, and $d_4$) as shown above in Fig. 6. Different configurations of the longitudinal steel reinforcement are tested in addition to a sample with transverse steel reinforcements. The steel reinforcements are located at the front and back surfaces of the slabs. The diameter used for all the longitudinal and transverse steel reinforcements is 6 mm. Six concrete samples were modeled under different striking velocities. The first sample represents the plain concrete without steel reinforcement (PCS). The second, third, fourth, and fifth samples represent the reinforced concrete samples with different configurations of longitudinal steel reinforcement which are illustrated, respectively, in Figs. 2(a) (NRCS), 9(a) (RCS1), 9(b) (RCS2), and 9(c) (RCS3). The sixth sample contains transverse steel reinforcement bars in addition to the normal reinforced concrete sample of Fig. 2(a) as shown in Fig. 9(d) (SRCS). In the sample NRCS the spacing mesh of the steel bars is 75 mm, while in the rest of the samples the spacing mesh is 37.5 mm. The minimum mesh spacing was resepcted such that the projectile diamteer is less than the mesh spacing between the steel bars in the impact zone. It should be noted that the mechanical properties of concrete and steel reinforcement are the same presented above in Tables 1 and 2. The residual velocity, cratering and
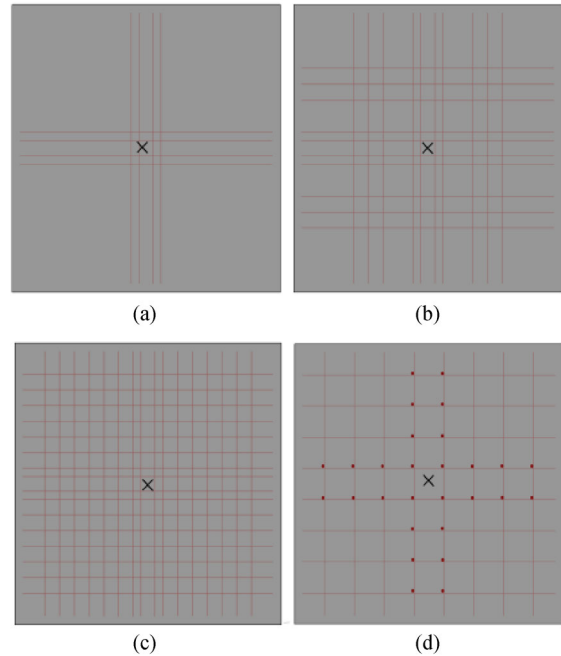


Fig. 9   Configurations of longitudinal and transverse reinforcement steels of (a) RCS1, (b) RCS2, (c) RCS3, (d) SRCS samples.

scabbing damages of each concrete sample are shown in Table 3 and Fig. 10. From Table 3, it is observed that there is negligible difference in the ballistic resistance between the samples CPS and NRCS. However, the ballistic resistance of the samples NRCS, RCS1, RCS2, RCS3 and SRCS are higher comparing to the ballistic resistance of the plain concrete sample PCS. The maximum difference of ballistic resistance of the normal reinforced concrete sample NRCS comparing to PCS is found to be 2.5%, while the maximum different in the ballistic resistance of all the reinforced concrete samples comparing to PCS is found in the case od RCS2 with 5.18% corresponding to the striking velocity 540 m/s. On the
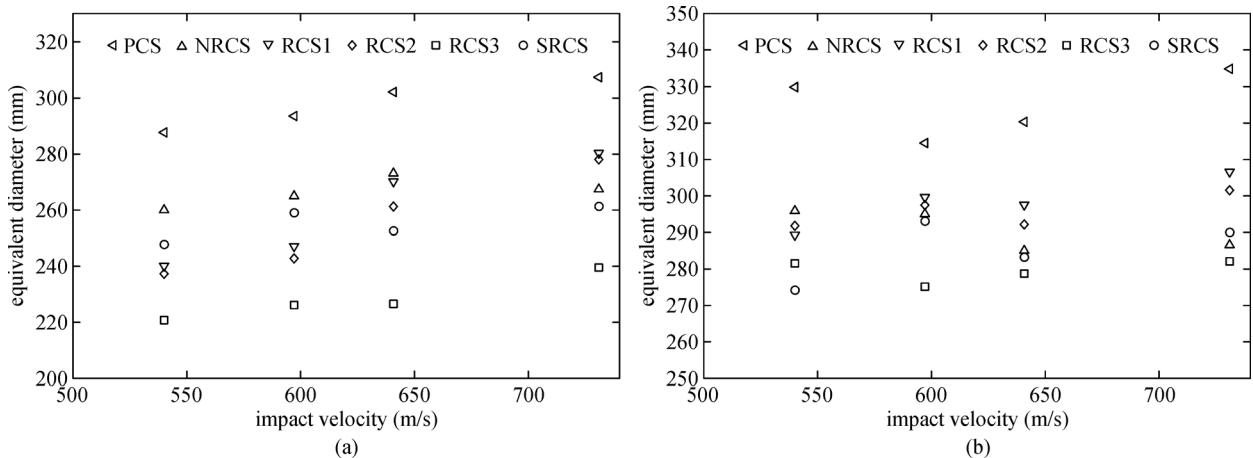


Fig. 10   Residual velocity and equivalent damage diameter of plain, reinforced and additionally reinforced concrete samples in (a) front surface and (b) back surface.

**Table 3** Residual velocity and equivalent damage diameter of plain, reinforced and additionally reinforced concrete samples

| sample | velocity | | front surface | | | | | back surface | | | | |
|---|---|---|---|---|---|---|---|---|---|---|---|---|
| | $V_0$ (m/s) | $V$ (m/s) | $d_1$ (mm) | $d_2$ (mm) | $d_3$ (mm) | $D_4$ (mm) | $d_m$ (mm) | $d_1$ (mm) | $d_2$ (mm) | $d_3$ (mm) | $D_4$ (mm) | $d_m$ (mm) |
| PCS | 540 | 308.71 | 287.57 | 298.16 | 280.07 | 285.40 | 287.80 | 321.96 | 337.23 | 327.81 | 332.16 | 329.79 |
| | 597 | 382.49 | 305.18 | 304.32 | 280.54 | 284.23 | 293.57 | 314.06 | 313.22 | 309.31 | 320.73 | 314.33 |
| | 641 | 439.15 | 301.66 | 312.22 | 295.64 | 299.03 | 302.14 | 323.87 | 318.45 | 324.51 | 313.63 | 320.12 |
| | 731 | 547.86 | 302.56 | 302.59 | 308.85 | 315.59 | 307.40 | 343.16 | 334.49 | 334.00 | 327.00 | 334.66 |
| NRCS | 540 | 307.24 | 284.80 | 281.40 | 235.5 | 238.20 | 259.98 | 318.4 | 306.97 | 278.93 | 278.75 | 295.76 |
| | 597 | 383.10 | 292.82 | 296.36 | 238.63 | 232.94 | 265.18 | 305.17 | 289.29 | 285.00 | 300.43 | 294.97 |
| | 641 | 439.36 | 299.95 | 301.71 | 246.89 | 244.04 | 273.15 | 298.14 | 295.76 | 276.25 | 270.19 | 285.09 |
| | 731 | 545.90 | 304.32 | 302.54 | 225.00 | 238.35 | 267.55 | 293.7 | 287.57 | 274.82 | 289.95 | 286.51 |
| RCS1 | 540 | 293.50 | 246.34 | 248.85 | 232.96 | 231.15 | 239.83 | 284.04 | 305.34 | 287.13 | 280.05 | 289.14 |
| | 597 | 375.21 | 262.97 | 262.92 | 239.89 | 221.90 | 246.92 | 288.37 | 302.64 | 298.19 | 308.24 | 299.36 |
| | 641 | 430.36 | 277.00 | 269.96 | 267.97 | 265.35 | 270.07 | 295.51 | 290.21 | 300.43 | 302.85 | 297.25 |
| | 731 | 537.94 | 277.00 | 280.53 | 277.10 | 286.72 | 280.34 | 320.4 | 305.18 | 302.85 | 297.48 | 306.48 |
| RCS2 | 540 | 293.50 | 246.34 | 245.31 | 233.60 | 224.62 | 237.46 | 284.96 | 301.66 | 284.95 | 294.79 | 291.59 |
| | 597 | 375.21 | 2262.96 | 260.37 | 238.36 | 219.31 | 242.75 | 285.74 | 297.22 | 303.22 | 303.91 | 297.52 |
| | 641 | 430.36 | 273.48 | 269.94 | 238.45 | 262.47 | 261.08 | 295.51 | 288.52 | 291.14 | 292.81 | 291.99 |
| | 731 | 537.94 | 277.00 | 277.00 | 276.68 | 281.37 | 278.01 | 309.57 | 303.45 | 294.89 | 297.53 | 301.36 |
| RCS3 | 540 | 297.08 | 241.78 | 246.32 | 190.44 | 204.78 | 220.83 | 282.39 | 287.57 | 274.71 | 281.21 | 281.47 |
| | 597 | 374.44 | 236.82 | 237.23 | 216.49 | 213.77 | 226.08 | 284.98 | 284.05 | 268.82 | 262.76 | 275.15 |
| | 641 | 430.62 | 236.82 | 235.79 | 219.20 | 213.77 | 226.40 | 301.69 | 298.14 | 257.67 | 257.37 | 278.72 |
| | 731 | 536.75 | 252.35 | 253.35 | 221.62 | 230.04 | 239.34 | 300.78 | 301.66 | 260.56 | 265.21 | 282.05 |
| SRCS | 540 | 301.40 | 283.25 | 282.51 | 211.68 | 213.88 | 247.83 | 304.35 | 302.62 | 243.60 | 246.26 | 274.21 |
| | 597 | 378.60 | 290.31 | 290.32 | 232.89 | 222.25 | 258.94 | 322.02 | 316.66 | 265.20 | 268.14 | 293.01 |
| | 641 | 433.33 | 295.61 | 292.10 | 214.23 | 208.58 | 252.63 | 304.49 | 302.61 | 262.56 | 263.43 | 283.27 |
| | 731 | 542.05 | 300.00 | 298.24 | 221.98 | 224.71 | 261.23 | 300.00 | 299.12 | 281.74 | 278.66 | 289.88 |

other hand, the normal reinforced concrete sample exhibits the maximum different in the ballistic resistance with the striking velocities 597, 641, and 731 m/s comparing to the sample PCS. It is also observed that the transverse steel reinforcements affect slightly the ballistic resistance when added to the normal reinforced concrete sample. It is also seen that for all the concrete samples the ballistic resistance increases with the decrease of the impact velocity. From Table 3, it is also observed that the equivalent damage diameter in the front and back surfaces of the reinforced concrete samples is lower than the equivalent damage diameter of plain concrete sample. On one hand, the equivalent damage diameter is found to decrease with the increase of the impact velocity. One can conclude that the ballistic resistance is mostly affected by the spacing mesh of steel reinforcement bars than the amount of steel reinforcement. Therefore, appropriate distribution of reinforcement is needed to reach a high ballistic resistance of steel reinforced concrete slabs. On the other hand, it can also be concluded that at high striking velocities the

amount of steel reinforcement can also be efficient to improve the ballistic resistance of concrete slabs.

## 6    Effect of projectile diameter

The effect of the ogive nosed projectile diameter on the ballistic resistance of the normal reinforced concrete sample NRCS is studied in this section. The projectile diameter was varied such that it takes the values 15, 25.3, and 30 mm as shown in Fig. 11. To ensure that the projectile will strike the concrete sample through impact, the maximum projectile diameter is taken such that is less than the mesh spacing of the longitudinal steel bars at the impact location. The mechanical properties of concrete and steel reinforcement are similar to the ones used in the previous sections. Figure 12 shows the variation of the residual velocity with different diameters of the projectiles. It is clearly shown that the residual velocity increases with the increase of the initial velocity and with the increase in
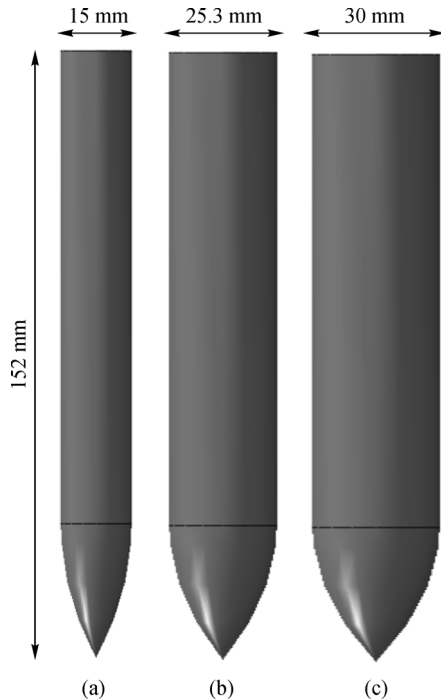
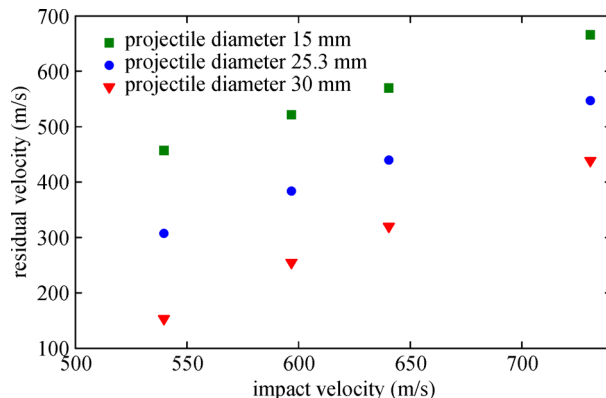**Fig. 11**   Various projectile diameters.



**Fig. 12**   Ballistic resistance of reinforced concrete sample with different projectile diameters.

the projectile diameter. It is concluded that the ballistic resistance is improved with the increase of the projectile diameter and the energy absorbed by the reinforced concrete slab is higher with the biggest projectile diameter and decreases with the decrease of the projectile diameter.

## 7    Conclusions

The Johnson-Holmquist-2 damage model was implemented for concrete material to study the behavior of plain and reinforced concrete slab under impact loads. The steel bars were modeled using the Johnson-Cook plasticity model and the ogive-nosed projectile was modeled as rigid body with a mass assigned at a reference point. The implemented impact model was validated and the numerical results showed good agreement with the experimental ones. Cratering and scabbing damages and residual velocity of plain and different reinforced concrete samples were compared in order to describe the effect of steel reinforcement on the ballistic resistance of the concrete samples. It was found that the added steel reinforcement to the concrete sample has significant influence on the ballistic resistance comparing to the plain concrete. On the other hand, it was found that the simple transverse reinforcement affects slightly the ballistic resistance of the concrete sample. It was also concluded that the ballistic resistance is mostly affected by the spacing mesh of the steel bars than the amount of the steel reinforcement in the concrete sample. However, at high striking velocity the amount of steel reinforcement can be efficient to improve the ballistic resistance of concrete slabs. The effect of projectile diameter was also studied in the present work in which it was found that the ballistic resistance and energy absorption of the reinforced concrete slab increase with the increase of the projectile diameter.

## References

1. Plotzitza A, Rabczuk T, Eibl J. Techniques for numerical simulations of concrete slabs for demolishing by blasting. Journal of Engineering Mechanics, 2007, 133(5): 523–533

2. Oucif C, Mauludin L M. Numerical modeling of high velocity impact applied to reinforced concrete panel. Underground Space, 2018, 4(1): 1–9

3. Rabczuk T, Akkermann J, Eibl J. A numerical model for reinforced concrete structures. International Journal of Solids and Structures, 2005, 42(5–6):1327–1354

4. Rabczuk T, Belytschko T. Application of particle methods to static fracture of reinforced concrete structures. International Journal of Fracture, 2006, 137(1–4): 19–49

5. Rabczuk T, Zi G, Bordas S, Nguyen-Xuan H. A geometrically non-linear three-dimensional cohesive crack method for reinforced concrete structures. Engineering Fracture Mechanics, 2008, 75(16): 4740–4758

6. Oucif C, Ouzaa K, Stoian V, Dăescu C A. Numerical modeling of reinforced concrete strengthened columns under cyclic loading. Arabian Journal for Science and Engineering, 2017, 42(9): 3933–3944

7. Oucif C, Ouzaa K, Mauludin L M. Cyclic and monotonic behavior of strengthened and unstrengthened square reinforced concrete

columns. Journal of Applied and Computational Mechanics, 2019, 5(3): 517–525

8. Rabczuk T, Eibl J. Modelling dynamic failure of concrete with meshfree methods. International Journal of Impact Engineering, 2006, 32(11): 1878–1897

9. Kalameh H A, Karamali A, Anitescu C, Rabczuk T. High velocity impact of metal sphere on thin metallic plate using smooth particle hydrodynamics (SPH) method. Frontiers of Structural and Civil Engineering, 2012, 6(2): 101–110

10. Diyaroglu C, Oterkus E, Madenci E, Rabczuk T, Siddiq A. Peridynamic modeling of composite laminates under explosive loading. Composite Structures, 2016, 144: 14–23

11. Hu F, Wu H, Fang Q, Liu J C, Liang B, Kong X Z. Impact performance of explosively formed projectile (EFP) into concrete targets. International Journal of Impact Engineering, 2017, 109: 150–166

12. Rabczuk T, Eibl J. Simulation of high velocity concrete fragmentation using SPH/MLSPH. International Journal for Numerical Methods in Engineering, 2003, 56(10): 1421–1444

13. Rabczuk T, Eibl J, Stempniewski L. Numerical analysis of high speed concrete fragmentation using a meshfree lagrangian method. Engineering Fracture Mechanics, 2004, 71(4–6): 547–556

14. Groeneveld A B, Ahlborn T M, Crane C K, Burchfield C A, Landis E N. Dynamic strength and ductility of ultra-high performance concrete with flow-induced fiber alignment. International Journal of Impact Engineering, 2018, 111: 37–45

15. Lu D, Wang G, Du X, Wang Y. A nonlinear dynamic uniaxial strength criterion that considers the ultimate dynamic strength of concrete. International Journal of Impact Engineering, 2017, 103: 124–137

16. Hanchak S J, Forrestal M J, Young E R, Ehrgott J Q. Perforation of concrete slabs with 48 MPa (7 ksi) and 140 MPa (20 ksi) unconfined compressive strengths. International Journal of Impact Engineering, 1992, 12(1): 1–7

17. Borvik T, Langseth M, Hopperstad O S, Polanco-Loria M A. Ballistic perforation resistance of high performance concrete slabs with different unconfined compressive strengths. WIT Transactions on the Built Environment, 2002, 59: 273–282

18. Cai J, Ye J, Wang Y, Chen Q. Numerical study on dynamic response of reinforced concrete columns under low-speed horizontal impact loading. Procedia Engineering, 2017, 210: 334–340

19. Li J, Wu C, Hao H, Su Y, Li Z X. A study of concrete slabs with steel wire mesh reinforcement under close-in explosive loads. International Journal of Impact Engineering, 2017, 110: 242–254

20. Liu J, Wu C, Li J, Su Y, Shao R, Liu Z, Chen G. Experimental and numerical study of reactive powder concrete reinforced with steel wire mesh against projectile penetration. International Journal of Impact Engineering, 2017, 109: 131–149

21. Isaac P, Darby A, Ibell T, Evernden M. Experimental investigation into the force propagation velocity due to hard impacts on reinforced concrete members. International Journal of Impact Engineering, 2017, 100: 131–138

22. Othman H, Marzouk H. An experimental investigation on the effect of steel reinforcement on impact response of reinforced concrete plates. International Journal of Impact Engineering, 2016, 88: 12–21

23. Thai D K, Kim S E, Bui T Q. Modified empirical formulas for predicting the thickness of RC panels under impact loading. Construction & Building Materials, 2018, 169: 261–275

24. Feng J, Song M, He Q, Sun W, Wang L, Luo K. Numerical study on the hard projectile perforation on RC panels with ldpm. Construction & Building Materials, 2018, 183: 58–74

25. Thai D K, Kim S E. Numerical investigation of the damage of RC members subjected to blast loading. Engineering Failure Analysis, 2018, 92: 350–367

26. Zhao D B, Yi W J, Kunnath S K. Numerical simulation and shear resistance of reinforced concrete beams under impact. Engineering Structures, 2018, 166: 387–401

27. Kong X, Fang Q, Wu H, Peng Y. Numerical predictions of cratering and scabbing in concrete slabs subjected to projectile impact using a modified version of HJC material model. International Journal of Impact Engineering, 2016, 95: 61–71

28. Kong X, Fang Q, Li Q M, Wu H, Crawford J E. Modified K&C model for cratering and scabbing of concrete slabs under projectile impact. International Journal of Impact Engineering, 2017, 108: 217–228

29. Kong X, Fang Q, Chen L, Wu H. A new material model for concrete subjected to intense dynamic loadings. International Journal of Impact Engineering, 2018, 120: 60–78

30. Navas P, Yu R C, Li B, Ruiz G. Modeling the dynamic fracture in concrete: An eigensoftening meshfree approach. International Journal of Impact Engineering, 2018, 113: 9–20

31. Rabczuk T, Belytschko T. Adaptivity for structured meshfree particle methods in 2D and 3D. International Journal for Numerical Methods in Engineering, 2005, 63(11): 1559–1582

32. Rabczuk T, Areias P M A, Belytschko T. A meshfree thin shell method for non-linear dynamic fracture. International Journal for Numerical Methods in Engineering, 2007, 72(5): 524–548

33. Rabczuk T, Belytschko T. A three-dimensional large deformation meshfree method for arbitrary evolving cracks. Computer Methods in Applied Mechanics and Engineering, 2007, 196(29–30): 2777–2799

34. Rabczuk T, Bordas S P A, Askes H. Meshfree Discretization Methods for Solid Mechanics. New Jersey: John Wiley & Sons, 2010

35. Zi G, Rabczuk T, Wall W. Extended meshfree methods without branch enrichment for cohesive cracks. Computational Mechanics, 2007, 40(2): 367–382

36. Bordas S, Rabczuk T, Zi G. Three-dimensional crack initiation, propagation, branching and junction in non-linear materials by an extended meshfree method without asymptotic enrichment. Engineering Fracture Mechanics, 2008, 75(5): 943–960

37. Amiri F, Millán D, Shen Y, Rabczuk T, Arroyo M. Phase-field modeling of fracture in linear thin shells. Theoretical and Applied Fracture Mechanics, 2014, 69: 102–109

38. Amiri F, Anitescu C, Arroyo M, Bordas S P A, Rabczuk T. XLME interpolants, a seamless bridge between XFEM and enriched meshless methods. Computational Mechanics, 2014, 53(1): 45–57

39. Fu Z J, Xi Q, Chen W, Cheng A H D. A boundary-type meshless solver for transient heat conduction analysis of slender functionally graded materials with exponential variations. Computers & Mathematics with Applications, 2018, 76(4): 760–773

40. Fu Z, Chen W, Wen P, Zhang C. Singular boundary method for

wave propagation analysis in periodic structures. Journal of Sound and Vibration, 2018, 425: 170–188

41. Rabczuk T, Zi G, Bordas S, Nguyen-Xuan H. A simple and robust three-dimensional cracking-particle method without enrichment. Computer Methods in Applied Mechanics and Engineering, 2010, 199(37–40): 2437–2455

42. Rabczuk T, Belytschko T. Cracking particles: A simplified meshfree method for arbitrary evolving cracks. International Journal for Numerical Methods in Engineering, 2004, 61(13): 2316–2343

43. Ren H, Zhuang X, Rabczuk T. Dual-horizon peridynamics: A stable solution to varying horizons. Computer Methods in Applied Mechanics and Engineering, 2017, 318: 762–782

44. Ren H, Zhuang X, Cai Y, Rabczuk T. Dual-horizon peridynamics. International Journal for Numerical Methods in Engineering, 2016, 108(12): 1451–1476

45. Areias P, Reinoso J, Camanho P P, César de Sá J, Rabczuk T. Effective 2D and 3D crack propagation with local mesh refinement and the screened Poisson equation. Engineering Fracture Mechanics, 2018, 189: 339–360

46. Areias P, Rabczuk T. Steiner-point free edge cutting of tetrahedral meshes with applications in fracture. Finite Elements in Analysis and Design, 2017, 132: 27–41

47. Areias P, Msekh M A, Rabczuk T. Damage and fracture algorithm using the screened poisson equation and local remeshing. Engineering Fracture Mechanics, 2016, 158: 116–143

48. Ghorashi S S, Valizadeh N, Mohammadi S, Rabczuk T. T-spline based XIGA for fracture analysis of orthotropic media. Computers & Structures, 2015, 147: 138–146

49. Areias P, Rabczuk T, Camanho P P. Finite strain fracture of 2D problems with injected anisotropic softening elements. Theoretical and Applied Fracture Mechanics, 2014, 72: 50–63

50. Areias P, Rabczuk T, Dias-da Costa D. Element-wise fracture algorithm based on rotation of edges. Engineering Fracture Mechanics, 2013, 110: 113–137

51. Areias P, Rabczuk T. Finite strain fracture of plates and shells with configurational forces and edge rotations. International Journal for Numerical Methods in Engineering, 2013, 94(12): 1099–1122

52. Chau-Dinh T, Zi G, Lee P S, Rabczuk T, Song J H. Phantom-node method for shell models with arbitrary cracks. Computers & Structures, 2012, 92–93: 242–256

53. Rabczuk T, Bordas S, Zi G. On three-dimensional modelling of crack growth using partition of unity methods. Computers & Structures, 2010, 88(23–24): 1391–1411

54. Rabczuk T, Gracie R, Song J H, Belytschko T. Immersed particle method for fluid-structure interaction. International Journal for Numerical Methods in Engineering, 2010, 81(1): 48–71

55. Mauludin L M, Oucif C. Interaction between matrix crack and circular capsule under uniaxial tension in encapsulation-based self-healing concrete. Underground Space, 2018, 3(3): 181–189

56. Mauludin L M, Oucif C. The effects of interfacial strength on fractured microcapsule. Frontiers of Structural and Civil Engineering, 2019, 13(2): 353–363

57. Oucif C, Voyiadjis G Z, Kattan P I, Rabczuk T. Nonlinear superhealing and contribution to the design of a new strengthening theory. Journal of Engineering Mechanics, 2018, 144(7): 04018055

58. Oucif C, Voyiadjis G Z, Rabczuk T. Modeling of damage-healing and nonlinear self-healing concrete behavior: Application to coupled and uncoupled self-healing mechanisms. Theoretical and Applied Fracture Mechanics, 2018, 96: 216–230

59. Oucif C, Voyiadjis G Z, Kattan P I, Rabczuk T. Investigation of the super healing theory in continuum damage and healing mechanics. International Journal of Damage Mechanics, 2018, 28(6): 896–917

60. Msekh M A, Cuong N H, Zi G, Areias P, Zhuang X, Rabczuk T. Fracture properties prediction of clay/epoxy nanocomposites with interphase zones using a phase field model. Engineering Fracture Mechanics, 2018, 188: 287–299

61. Amani J, Oterkus E, Areias P, Zi G, Nguyen-Thoi T, Rabczuk T. A non-ordinary state-based peridynamics formulation for thermoplastic fracture. International Journal of Impact Engineering, 2016, 87: 83–94

62. Gui Y L, Bui H H, Kodikara J, Zhang Q B, Zhao J, Rabczuk T. Modelling the dynamic failure of brittle rocks using a hybrid continuum-discrete element method with a mixed-mode cohesive fracture model. International Journal of Impact Engineering, 2016, 87: 146–155

63. Talebi H, Silani M, Rabczuk T. Concurrent multiscale modeling of three dimensional crack and dislocation propagation. Advances in Engineering Software, 2015, 80: 82–92

64. Talebi H, Silani M, Bordas S P A, Kerfriden P, Rabczuk T. A computational library for multiscale modeling of material failure. Computational Mechanics, 2014, 53(5): 1047–1071

65. Budarapu P R, Gracie R, Bordas S P A, Rabczuk T. An adaptive multiscale method for quasi-static crack growth. Computational Mechanics, 2014, 53(6): 1129–1148

66. Budarapu P R, Gracie R, Yang S W, Zhuang X, Rabczuk T. Efficient coarse graining in multiscale modeling of fracture. Theoretical and Applied Fracture Mechanics, 2014, 69: 126–143

67. Zhou S, Zhuang X, Zhu H, Rabczuk T. Phase field modelling of crack propagation, branching and coalescence in rocks. Theoretical and Applied Fracture Mechanics, 2018, 96: 174–192

68. Zhou S, Zhuang X, Rabczuk T. A phase-field modeling approach of fracture propagation in poroelastic media. Engineering Geology, 2018, 240: 189–203

69. Zhou S, Rabczuk T, Zhuang X. Phase field modeling of quasi-static and dynamic crack propagation: COMSOL implementation and case studies. Advances in Engineering Software, 2018, 122: 31–49

70. Zhou S W, Xia C C. Propagation and coalescence of quasistatic cracks in Brazilian disks: An insight from a phase field model. Acta Geotechnica, 2018, 14: 1195–1214

71. Areias P, Rabczuk T, Msekh M A. Phase-field analysis of finite-strain plates and shells including element subdivision. Computer Methods in Applied Mechanics and Engineering, 2016, 312: 322–350

72. Badnava H, Etemadi E, Msekh M. A phase field model for rate-dependent ductile fracture. Metals, 2017, 7(5): 180

73. Liu G, Li Q, Msekh M A, Zuo Z. Abaqus implementation of monolithic and staggered schemes for quasi-static and dynamic fracture phase-field model. Computational Materials Science, 2016, 121: 35–47

74. Msekh M A, Silani M, Jamshidian M, Areias P, Zhuang X, Zi G, He P, Rabczuk T. Predictions of J integral and tensile strength of clay/epoxy nanocomposites material using phase field model. Compo-

sites. Part B, Engineering, 2016, 93: 97–114

75. Msekh M A, Sargado J M, Jamshidian M, Areias P M, Rabczuk T. Abaqus implementation of phase-field model for brittle fracture. Computational Materials Science, 2015, 96: 472–484

76. Hamdia K M, Msekh M A, Silani M, Vu-Bac N, Zhuang X, Nguyen-Thoi T, Rabczuk T. Uncertainty quantification of the fracture properties of polymeric nanocomposites based on phase field modeling. Composite Structures, 2015, 133: 1177–1190

77. Johnson G R, Holmquist T J. A Computational Constitutive Model for Brittle Materials Subjected to Large Strains, High Strain Rates and High Pressures. New York: Marcel Dekker Inc., 1992

78. Rosenberg Z. On the relation between the hugoniot elastic limit and the yield strength of brittle materials. Journal of Applied Physics, 1993, 74(1): 752–753

79. Johnson G R, Cook W H. Fracture characteristics of three metals subjected to various strains, strain rates, temperatures and pressures. Engineering Fracture Mechanics, 1985, 21(1): 31–48

80. Ãrvik T B, Hopperstad O S, Berstad T, Langseth M. Numerical simulation of plugging failure in ballistic penetration. International Journal of Solids and Structures, 2001, 38(34): 6241–6264

81. Wu H, Fang Q, Peng Y, Gong Z M, Kong X Z. Hard projectile perforation on the monolithic and segmented RC panels with a rear steel liner. International Journal of Impact Engineering, 2015, 76: 232–250